THE AMERICAN SOCIETY OF MECHANICAL ENGINEERS
345 E. 47th St., New York, N.Y. 10017

97-GT-68

NUMERICAL ANALYSIS OF TRANSONIC COMPRESSOR ROTOR FLOW NEAR STALL POINTS

Daisaku Masaki
Kawasaki Heavy Industries, Ltd.
Akashi, Japan

Shojiro Kaji
University of Tokyo
Tokyo, Japan

ABSTRACT

A three-dimensional Navier-Stokes solver based upon a high resolution shock-capturing scheme has been developed in order to analyze complex flow phenomena inside transonic fan/compressor rotors, especially tip clearance flow. The aim of this research is to find out a key element concerned with aerodynamic instability of transonic fan/compressor rotors such as rotating stall and surge by using this newly developed numerical tool. The numerical analysis of this research is twofold. First it investigates the flowfield of a transonic compressor rotor along the design speed operating line. It obtains definite flow structures around the tip region and clear description of the transition of the flow pattern inside the clearance gap between operating points, which shows that shock-tip leakage vortex interaction plays an important role on both loss generation and the failure of steady flow, or surge. A model will be proposed on the onset of tip stall in transonic compressor rotors according to the calculated results.

Secondly, the above model will be examined through a series of numerical experiments by altering tip clearance height while keeping the design speed. From qualitative point of view, the model works fairly well and seems geometry-independent for typical transonic fan/compressor rotors. A clue to the optimum clearance is also obtained.

INTRODUCTION

A variety of phenomena complicate the flowfield inside modern transonic fan/compressor rotors. These phenomena are; three-dimensional multi-shock structure, shock-boundary layer interaction, radial flow migration inside the boundary layer caused by centrifugal force and tip clearance flow. Among them the tip clearance flow has a dominant influence on both efficiency and stability of fan/compressor rotors and this fact has been confirmed by measurements (e.g. Freeman, 1985, Wisler, 1985, etc.). Hence understanding the detail of the flowfield around the tip region is essential to specify the loss generation mechanism and stability bounds of modern fan/compressor rotors. However, conventional analytical and experimental methods having various constraints cannot look into those complex flow phenomena inside rotors. Although LDV (Laser Doppler Velocimeter) may be the only experimental technique to measure flow features in machines running at high speeds, it cannot avoid certain limitations, either. For example, blade geometry may be an obstruction itself to the glancing angle. Compliance of the seeds to flow is always a controversial problem. Scattering of the laser by blade surfaces and casing endwalls degrades the accuracy of the measured data around them and makes it difficult to investigate flow features in these high loss regions. Distribution of the seeds to the region of subtle flow phenomena like boundary layer and tip clearance flow in high speed machines is always not enough. Strazisar et al. (1989) have conducted successfully the first and the only extensive laser measurements in a low aspect ratio transonic fan. Their measurements have obtained the flow patterns near peak efficiency and near stall at experimentally not so severe radial positions. Nevertheless even their close examinations could not measure the tip clearance flow.

Presented at the International Gas Turbine & Aeroengine Congress & Exhibition
Orlando, Florida — June 2–June 5, 1997

On the other hand, numerical analysis has been able to provide an alternative tool to analyze turbomachinery flow in the last decade. The works of Dawes (1988), Chima and Yokota (1990), Weber and Delaney (1991), Hah and Reid (1992), Jennions and Turner (1993), and Arnone (1994) are typical state-of-the-art three-dimensional viscous flow analysis tools in the area of turbomachinery. These analyses exhibited sufficient quantitative accuracy for design use and reproduced the measured flowfield successfully and accurately. But there have been fewer publications of the calculated results on the flowfield in the tip gap region. So far as the present authors know, the numerical analyses which show flowfields in the tip gap region inside transonic fan/compressor rotors in the open literature are those of Hah and Wennerstrom (1991), Adamczyk et al. (1993), Jennions and Turner (1993), Arnone (1994), and Chima (1996). Although the current work owes much to their papers, in our opinion their computed results do not describe clearly the flow patterns expressed in Mach number contours or do not explain the detailed flow physics precisely. Therefore, this research analyzes numerically the detailed flowfield inside a transonic compressor rotors, placing particular emphasis on obtaining clear description of flow pattern and definite explanation of flow physics in the tip gap region where experimental methods can hardly be applied, and tries to make clear the process of the onset of aerodynamic instability occurring near the surge line. Our final object is to extract from calculated results some model on the onset of aerodynamic instability of transonic fan/compressor rotors and to validate it. We start with a relatively simple model deduced from simplified calculations, conduct more sophisticated calculations and experiments based upon the model, compare the obtained results, eliminate or modify some, and improve the model. We believe this approach will enable us to reach the truth faster than random approaches. This paper describes the first step of this approach.

THE NUMERICAL PROCEDURE

The Governing Equations

The governing equations are three-dimensional, unsteady, Reynolds-averaged full Navier-Stokes equations cast in the relative frame of reference rotating around the x-axis with constant angular velocity Ω. They are summarized in the conservation form in a curvilinear transformation as follows.

$$\frac{\partial \hat{Q}}{\partial t} + \frac{\partial \hat{E}}{\partial \xi} + \frac{\partial \hat{F}}{\partial \eta} + \frac{\partial \hat{G}}{\partial \zeta} = \frac{\partial \hat{E}_v}{\partial \xi} + \frac{\partial \hat{F}_v}{\partial \eta} + \frac{\partial \hat{G}_v}{\partial \zeta} + \hat{T} \qquad (1)$$

Let ρ, u, v, w, e and p denote density, cartesian velocity components in the x, y and z directions, total energy per unit volume and pressure respectively, then the dependent variables and the inviscid flux terms are written in the vector form as,

$$\hat{Q} = J^{-1}\begin{bmatrix}\rho\\ \rho u\\ \rho v\\ \rho w\\ e\end{bmatrix},\ \hat{E} = J^{-1}\begin{bmatrix}\rho U\\ \rho uU + \xi_x p\\ \rho vU + \xi_y p\\ \rho wU + \xi_z p\\ (e+p)U - \xi_t p\end{bmatrix},\ \hat{F} = J^{-1}\begin{bmatrix}\rho V\\ \rho uV + \eta_x p\\ \rho vV + \eta_y p\\ \rho wV + \eta_z p\\ (e+p)V - \eta_t p\end{bmatrix} \qquad (2a)$$

$$\hat{G} = J^{-1}\begin{bmatrix}\rho W\\ \rho uW + \zeta_x p\\ \rho vW + \zeta_y p\\ \rho wW + \zeta_z p\\ (e+p)W - \zeta_t p\end{bmatrix},\ \hat{T} = J^{-1}\begin{bmatrix}0\\ 0\\ \Omega\rho w\\ -\Omega\rho v\\ 0\end{bmatrix} \qquad (2b)$$

U, V, W are contravariant velocity components and defined as

$$\begin{aligned} U &= \xi_t + \xi_x u + \xi_y v + \xi_z w\\ V &= \eta_t + \eta_x u + \eta_y v + \eta_z w\\ W &= \zeta_t + \zeta_x u + \zeta_y v + \zeta_z w \end{aligned} \qquad (3)$$

where

$$\begin{aligned} \xi_t &= \Omega(\xi_y z - \xi_z y)\\ \eta_t &= \Omega(\eta_y z - \eta_z y)\\ \zeta_t &= \Omega(\zeta_y z - \zeta_z y) \end{aligned} \qquad (4)$$

The viscous flux terms are arranged into a similar vector form as;

$$\hat{E}_v = J^{-1}\begin{bmatrix}0\\ \xi_x\tau_{xx} + \xi_y\tau_{xy} + \xi_z\tau_{xz}\\ \xi_x\tau_{yx} + \xi_y\tau_{yy} + \xi_z\tau_{yz}\\ \xi_x\tau_{zx} + \xi_y\tau_{zy} + \xi_z\tau_{zz}\\ \xi_x\beta_x + \xi_y\beta_y + \xi_z\beta_z\end{bmatrix}\quad \hat{F}_v = J^{-1}\begin{bmatrix}0\\ \eta_x\tau_{xx} + \eta_y\tau_{xy} + \eta_z\tau_{xz}\\ \eta_x\tau_{yx} + \eta_y\tau_{yy} + \eta_z\tau_{yz}\\ \eta_x\tau_{zx} + \eta_y\tau_{zy} + \eta_z\tau_{zz}\\ \eta_x\beta_x + \eta_y\beta_y + \eta_z\beta_z\end{bmatrix} \qquad (5a)$$

$$\hat{G}_v = J^{-1}\begin{bmatrix}0\\ \zeta_x\tau_{xx} + \zeta_y\tau_{xy} + \zeta_z\tau_{xz}\\ \zeta_x\tau_{yx} + \zeta_y\tau_{yy} + \zeta_z\tau_{yz}\\ \zeta_x\tau_{zx} + \zeta_y\tau_{zy} + \zeta_z\tau_{zz}\\ \zeta_x\beta_x + \zeta_y\beta_y + \zeta_z\beta_z\end{bmatrix} \qquad (5b)$$

where,

$$\begin{aligned} \tau_{xx} &= 2\mu u_x - \lambda\mu(u_x + v_y + w_z)\\ \tau_{yy} &= 2\mu v_y - \lambda\mu(u_x + v_y + w_z)\\ \tau_{zz} &= 2\mu w_z - \lambda\mu(u_x + v_y + w_z)\\ \tau_{xy} &= \tau_{yx} = \mu(u_y + v_x)\\ \tau_{yz} &= \tau_{zy} = \mu(v_z + w_y)\\ \tau_{zx} &= \tau_{xz} = \mu(w_x + u_z)\\ \beta_x &= u\tau_{xx} + v\tau_{xy} + w\tau_{xz} + \kappa T_x\\ \beta_y &= u\tau_{yx} + v\tau_{yy} + w\tau_{yz} + \kappa T_y\\ \beta_z &= u\tau_{zx} + v\tau_{zy} + w\tau_{zz} + \kappa T_z \end{aligned} \qquad (6)$$

The first derivatives in (6) are evaluated in a non-conservative way,

using the curvilinear coordinate system and its chain rules.
The static pressure is coupled with the dependent variables through the equation of state;

$$p = (\gamma - 1)[e - 1/2\rho(u^2 + v^2 + w^2)] \tag{7}$$

In the above notations, Stokes' hypothesis is assumed to be valid, that is, $\lambda = -2/3\mu$ and the Boussinesq hypothesis is adopted. Thus, the molecular viscosity μ and molecular thermal conductivity κ are replaced with;

$$\mu \rightarrow \mu_l + \mu_t \tag{8}$$

$$\kappa \rightarrow c_p\left(\frac{\mu_l}{Pr_l} + \frac{\mu_t}{Pr_t}\right) \tag{9}$$

where c_p is the specific heat at constant pressure and Pr is the Prandtl number. The subscripts l and t denote laminar and turbulent quantities respectively. The molecular viscosity μ_l is determined by Sutherland's law. The turbulent viscosity is evaluated with Baldwin-Lomax two-layer mixing length model (Baldwin and Lomax, 1978) modified by Chima (Chima et al., 1993). The model is applied separately along a grid line in the blade-to-blade direction and in the spanwise direction. The effect of multiple walls at corners and in the clearance gap regions is accounted for by using the blending function similar to the one used by Arnone (1994). In all calculations shown below, the laminar and turbulent Prandtl numbers are kept constant, and taken to be 0.72 and 0.90, respectively.

The non-MUSCL-type TVD Formulation

The numerical method adopted for this study is non-MUSCL-type TVD (Total Variation Diminishing) scheme of Yee and Harten (1987) based upon Roe's approximate Riemann solver. The two-parameter family of TVDschemes enhanced by Yee et al. (1990) in two-dimensional hypersonic viscous flow calculations has been extended for three-dimensional turbomachinery calculations by the first author of the present paper (Masaki and Kaji, 1994; Masaki, 1995). Only the formulation in the ξ-terms are shown below. The numerical flux function of the non-MUSCL-type TVD scheme is written as follows;

$$\begin{aligned}\hat{E}_{j+1/2,kl} = \frac{1}{2}\Bigg[&\left(\frac{\xi_y}{J}\right)_{j+1/2}(Q_{jkl} + Q_{j+1,kl}) + \left(\frac{\xi_z}{J}\right)_{j+1/2}(E_{jkl} + E_{j+1,kl}) \\ &+ \left(\frac{\xi_y}{J}\right)_{j+1/2}(F_{jkl} + F_{j+1,kl}) + \left(\frac{\xi_z}{J}\right)_{j+1/2}(G_{jkl} + G_{j+1,kl}) \\ &+ R_{j+1/2}\Phi_{j+1/2}/J_{j+1/2}\Bigg]\end{aligned} \tag{10}$$

where the subscripts j, k, l denote the grid indices in the ξ, η, ζ directions. Note that discretization is performed via a finite volume cell-vertex method, although expressions in Eqs. (2)~(5) use the general curvilinear transformations. E, F and G are fluxes in the x-, y- and z- directions. Here R is the right eigen vectors of the Jacobian matrix $\partial\hat{E}/\partial\hat{Q}$. The second-order upwind scheme is used. The elements of $\Phi_{j+1/2}$ are ;

$$\phi^l_{j+1/2} = \frac{1}{2}\psi(a^l_{j+1/2})(g^l_j + g^l_{j+1}) - \psi(a^l_{j+1/2} + \gamma^l_{j+1/2})\alpha^l_{j+1/2} \tag{11}$$

and

$$\gamma^l_{j+1/2} = \frac{1}{2}\psi(a^l_{j+1/2})\begin{cases}(g^l_{j+1} - g^l_j)/\alpha^l_j & \alpha^l_{j+1/2} \neq 0 \\ 0 & \alpha^l_{j+1/2} = 0\end{cases} \tag{12}$$

where a^l are the characteristic speeds of the Jacobian matrix $\partial\hat{E}/\partial\hat{Q}$ and $\alpha^l_{j+1/2}$ are "wave strength" and are components of

$$\alpha_{j+1/2} = R^{-1}_{j+1/2}(Q_{j+1,kl} - Q_{jkl}) \tag{13}$$

All the terms in $R_{j+1/2}\Phi_{j+1/2}$ are evaluated with Roe averaged values (Roe, 1981). g^l are limiter functions. In this study, different limiters are used for convective waves and for acoustic waves. For acoustic waves, in order to capture complex multi-shock structure clearly, van Leer's "Monotonized Central Difference" limiter is used. Its definition is expressed as;

$$g^l_j = \min \text{mod}(2\alpha^l_{j+1/2}, 2\alpha^l_{j-1/2}, 1/2(\alpha^l_{j+1/2} + \alpha^l_{j-1/2})) \tag{14}$$

For convective waves, in order to capture slip flows and thin shear layers without smearing, Roe's "Superbee" limiter is used. Its definition is as follows;

$$g^l_j = S\cdot\max(0, \min(2|\alpha^l_{j+1/2}|, S\cdot\alpha^l_{j-1/2}), \min(|\alpha^l_{j+1/2}|, 2S\cdot\alpha^l_{j-1/2})) \tag{15}$$

where $S = sgn(\alpha^l_{j+1/2})$. These limiters are more compressive than the conventional minmod limiter. ψ is an entropy correction function to prevent unphysical expansion shocks. It is expressed as;

$$\psi(z) = \begin{cases}|z| & |z| \geq \delta_1 \\ \dfrac{z^2 + \delta_1^2}{2\delta_1} & |z| \leq \delta_1\end{cases} \tag{16}$$

where δ_1 is a cutoff parameter. In order to enhance computational stability in high aspect ratio cells near solid walls common in the Navier-Stokes computations and to keep the amount of numerical dissipation as low as possible at the same time, the cutoff parameter originally devised by Martinelli (Martinelli and Jameson, 1988) and later applied successfully to non-MUSCL TVD schemes in two-dimensional hypersonic flow calculations by Müller (1989) is

simply extended to a three-dimensional form and employed;

$$\delta_i = \bar{\delta}\lambda_\xi\left\{1+\left(\frac{\lambda_\eta}{\lambda_\xi}\right)^\sigma+\left(\frac{\lambda_\zeta}{\lambda_\xi}\right)^\sigma\right\} \tag{17}$$

Here λ_ξ, *etc* are spectral radii of Jacobian matrices of inviscid fluxes and written as

$$\lambda_\xi = |U| + c\sqrt{\xi_x^2+\xi_y^2+\xi_z^2} \tag{18}$$

, etc., where c is the speed of sound. The exponent σ is usually chosen from $1/2 \le \sigma \le 1$. In all the calculations presented below, the value of 0.5 is enough to maintain robustness and accuracy. The entropy parameter $\bar{\delta}$ is set equal to 0.15 and is not altered throughout this study. The numerical flux functions $\bar{F}_{j,k+1/2,l}$ and $\bar{G}_{j,k,l+1/2}$ can be defined in a similar manner

As an implicit operator in the L.H.S., LCI (Linearized Conservative Implicit) form with full matrix formulation is used. This can be expressed as;

$$\left[I+\frac{\lambda^\xi\theta}{1+\omega}(H^\xi_{j+1/2,k,l}-H^\xi_{j-1/2,k,l})\right]^n D^{**} = \text{R.H.S.} \tag{19}$$

where

$$\begin{aligned}\text{R.H.S.} = &-\frac{\lambda^\xi}{1+\omega}[\bar{E}^n_{j+1/2,k,l}-\bar{E}^n_{j-1/2,k,l}]-\frac{\lambda^\eta}{1+\omega}[\bar{F}^n_{j,k+1/2,l}-\bar{F}^n_{j,k-1/2,l}]\\ &-\frac{\lambda^\zeta}{1+\omega}[\bar{G}^n_{j,k,l+1/2}-\bar{G}^n_{j,k,l-1/2}]+\frac{\Delta t}{1+\omega}\bar{T}^n_{j,k,l}+\frac{\omega}{1+\omega}\Delta\bar{Q}^{n-1}_{j,k,l}\end{aligned} \tag{20}$$

, the superscript n denotes the time index and $\lambda^\xi = \Delta t / \Delta\xi$, *etc*. Note that R.H.S. is an explicit numerical approximation to the steady part of the governing equations.

$$\left[I+\frac{\lambda^\eta\theta}{1+\omega}(H^\eta_{j,k+1/2,l}-H^\eta_{j,k-1/2,l})\right]^n D^{*} = D^{**} \tag{21}$$

$$\left[I+\frac{\lambda^\zeta\theta}{1+\omega}(H^\zeta_{j,k,l+1/2}-H^\zeta_{j,k,l-1/2})\right]^n D^{n} = D^{*} \tag{22}$$

$$D^n = \Delta\bar{Q}^n; \qquad \bar{Q}^{n+1} = \bar{Q}^n + D^n \tag{23}$$

The above scheme is second-order accurate in time if $\theta = \omega + 1/2$ and first-order accurate otherwise. H^ξ, *etc* in Eqs. (19) ~ (23) are written as

$$H^\xi_{j-1/2,k,l}D^{**} = \frac{1}{2}\left[\bar{\hat{A}}_{j+1,k,l}D^{**}_{j+1,k,l}+\bar{\hat{A}}_{j,k,l}D^{**}_{j,k,l}-\Omega^\xi_{j-1/2,k,l}D^{**}\right] \tag{24}$$

where

$$\bar{\hat{A}}_{j,k,l} = \left[\left(\frac{\xi_t}{J}\right)_{j+1/2}+\left(\frac{\xi_x}{J}\right)_{j+1/2}A_{j,k,l}+\left(\frac{\xi_y}{J}\right)_{j+1/2}B_{j,k,l}+\left(\frac{\xi_z}{J}\right)_{j+1/2}C_{j,k,l}\right]J_{j,k,l} \tag{25}$$

and,

$$\bar{\hat{A}}_{j-1,k,l} = \left[\left(\frac{\xi_t}{J}\right)_{j-1/2}+\left(\frac{\xi_x}{J}\right)_{j-1/2}A_{j-1,k,l}+\left(\frac{\xi_y}{J}\right)_{j-1/2}B_{j-1,k,l}+\left(\frac{\xi_z}{J}\right)_{j-1/2}C_{j-1,k,l}\right] \times J_{j-1,k,l} \tag{26}$$

Note that flux Jacobians A, B, C are defined as $\partial E / \partial Q$, $\partial F / \partial Q$, and $\partial G / \partial Q$ respectively. The full-matrix form of the difference operator Ω^ξ is used; thus

$$\Omega^\xi_{j+1/2,k,l}D^{**} = R_{j+1/2,k,l}\,\text{diag}\,[\psi(a^l_{j+1/2})]R^{-1}_{j+1/2,k,l}(D^{**}_{j+1,k,l}-D^{**}_{j,k,l}) \tag{27}$$

which was shown more effective in viscous flow computations (Yee et al., 1990).

Boundary Conditions

The governing equations are solved over one pitch of rotating blade passages on the assumption that the flow in each blade row is periodic. There are seven boundaries in the computational domain in three-dimensional cascade flow calculations. Those are inlet, outlet, periodic, blade surface, hub and casing walls. Since tip clearance is accounted for in this study, tip clearance boundary is also imposed. At the inlet, according to the one-dimensional theory of characteristics , total pressure, total temperature, radial and whirl velocity are specified and upstream-running Riemann invariant based upon total velocity

$$R^- = q - \frac{2c}{\gamma-1}, \quad q = \sqrt{u^2+v^2+w^2} \tag{28}$$

is extrapolated from the interior. Isentropic relations are used to obtain dependent variables. At the outlet, on the contrary, pressure is prescribed and ρ, u, v, w are extrapolated from the interior. Radial distribution of pressure is determined from the simple radial equilibrium

$$\frac{\partial p}{\partial r} = \frac{\rho v_\theta^2}{r} - \frac{\rho v_r^2}{r} - \frac{\partial \rho v_r^2}{\partial r} \tag{29}$$

with the prescribed value of pressure at the casing. Blade surface, hub and casing boundaries are solid walls and non-slip condition is imposed. That is, $U = V = W = 0$ for the blade surface and hub wall while $u = v = w = 0$ for the stationary casing wall. The pressure is extrapolated from the interior using the normal momentum equation along with the velocity components previously obtained. For the blade surface, it is expressed as

$$(\xi_x\eta_x + \xi_y\eta_y + \xi_z\eta_z)p_t + (\eta_x^2 + \eta_y^2 + \eta_z^2)p_\eta + (\eta_x\zeta_x + \eta_y\zeta_y + \eta_z\zeta_z)p_\zeta = \rho\Omega(\eta_y w - \eta_z v) \quad (30)$$

Similarly the normal momentum equations for the hub and casing walls is derived by interchanging η with ζ. Density is obtained from a temperature condition and all the walls are assumed to be adiabatic. Enforcing the periodicity may prevent the unsteady non-uniform disturbances from propagating circumferentially. Thus phenomena such as rotating stall cannot be analyzed under periodicity condition. As we assume that a surge line on a compressor characteristic map stands for limiting values at which periodic steady flow breaks down, and focus our research on the mechanism of the onset of unsteady flow, introduction of the periodic boundary and approach to the surge line from the steady flow side is justified. So the flow variables coincide at corresponding upper and lower periodic grid points. Tip clearance boundary is handled in a similar manner by imposing periodicity across the blade tip.

The more detailed implementation of the numerical procedure is given by Masaki (1995).

Computational Grid

Three-dimensional grids are generated analytically. First blade-to-blade two-dimensional grids are generated on arbitrary surfaces of revolution by an elliptic grid generator whose algorithm basically follows that by Sorenson (1981). Periodic C-type grids are used and orthogonality at the blade surface and smooth conjunction across the periodic boundary are enforced, using the forcing function. These blade-to-blade grids are stacked in the radial directions and their spanwise distributions are determined using hyperbolic tangent stretching to account for boundary layers on both endwalls. Figure 1 shows the 155 x 31 x 31 periodic C-type grid used for this study. Because of the constraints on computer storage available to us (210MB), the number of grid points could not be increased any more. As a result, we were forced to use rather coarse grids for this type of study. In the clearance gap, degenerate C-type grids generated around blades without thickness were filled. Thus, the blade tip was pinched within one grid point in the spanwise direction and the influence of tip geometry on limiting stream lines across the tip was expected to be minimum. Two or four cells were placed there according to tip clearance height.

Some preliminary calculations were conducted to examine dependency of solutions on grid density with more refined mesh (185 x 45 x 49) at a few operating points. The results showed that the shock locations and the location of the "edge" of the tip clearance flow (its definition will be addressed later) was little affected by grid density, but the radius of tip leakage vortex slightly changed because the geometry of the pinched tip was slightly altered. So we are convinced that the results will not be varied qualitatively with finer grids, and that the results obtained with this relatively coarse grid have a limited, qualitative validity, especially in terms of relative comparisons between the calculated results.

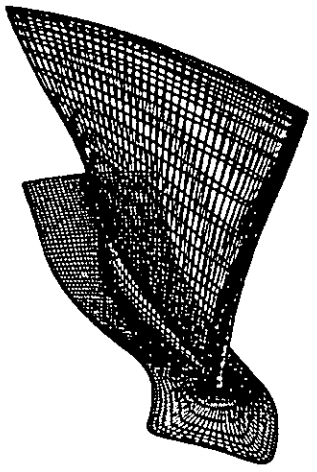

Fig. 1 155 X 31 X 31 Viscous Grid for a Transonic Compressor Rotor

Table. 1 Specifications of a Transonic Compressor Rotor

number of blade	24
design speed	49000 r.p.m.
mass flow rate	2.54 kg/s
total pressure ratio	1.7

The current study used the temporally second-order three-point backward differentiation ($\theta = 1, \varpi = 1/2$ in Eqs. (19)~(22)) time-differencing. All the calculations were started impulsively from the initial condition with uniform inlet hub values, and advanced in time with a sequence of fixed time step (Yee et al., 1990) together with second-order time-differencing until a steady solution, if it existed, was reached. Solutions were assumed to be converged to a steady state when L_2-norm of residuals had dropped by more than four orders of magnitude from initial one. The combination of second-order accurate time-differencing and fixed time step sequencing is not only shown to be effective in viscous steady calculations, but can give physical transient solutions while first-order time-accurate schemes with local-time step procedure cannot. This property of the present scheme is expected to be a superior one to trace the causes of unsteadiness.

RESULTS AND DISCUSSIONS

A Transonic Compressor Rotor

The numerical analyses have been conducted extensively on a low aspect ratio transonic compressor rotor. The specifications of the rotor are summarized in Table. 1 and its configuration is also seen from Fig. 1. This is the first stage rotor of a research turboshaft engine. Because the rotor was relatively small, the detailed measurement of the flowfield inside this rotor has not been

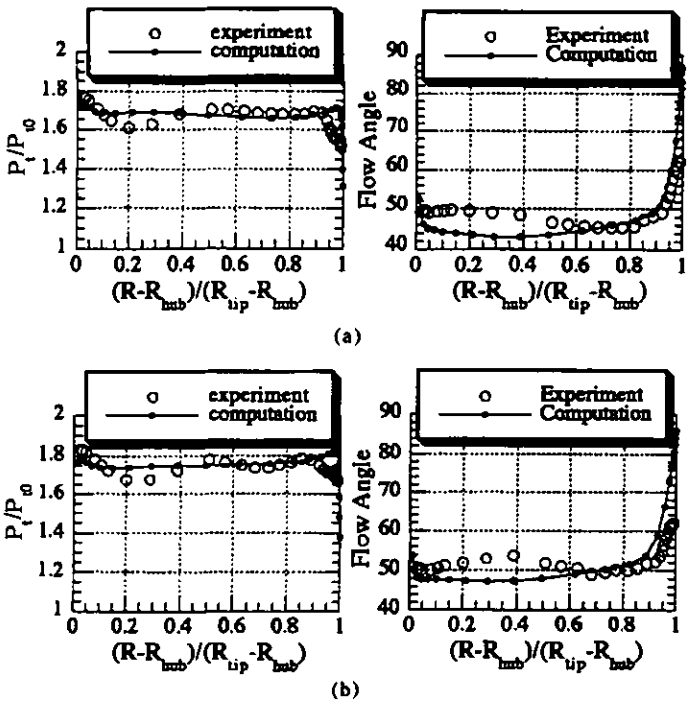

Fig. 2 Computed and Measured Exit Data with the Mass Flow Rate of (a) 2.73kg/s and of (b) 2.6kg/s; 0.5% Tip Clearance, Design Speed

carried out. Therefore, the thorough calibration of the current code is not conducted yet. The comparison with experiments in terms of spanwise distribution of the outlet total pressure and the flow angle at an exit plane at two operating points was made (Fig. 2). At a glance, discrepancy near endwalls is especially large. This was traced back to the fact that the actual rotor has 31 inlet guide vanes and resultant circumferentially non-uniform thick endwall layers, while the computations were performed on a single rotor with uniform inlet condition. As for quantitative accuracy of the code, nothing can be mentioned from these figures. But the rate of change of these variables caused by the transition of the operating point is fairly well predicted. This property is supposed to be important in comparisons between the calculated results.

The Transition of Flowfield inside the Clearance Gap along a Design Speed Line (0.5% Tip Clearance)

Due to space limitations, we cannot present all the calculated three-dimensional results and only the flow pattern inside the clearance gap is shown below.

The Flowfield at the Choke Point. The calculated choke mass flow rate was 2.76kg/s. Figure 3(a) shows relative Mach number contours inside the clearance gap which clearly exhibit the flow pattern at this condition. We can see that the tip clearance flow bursts out as a jet into a blade passage from the forward portion of the blade tip suction surface. Note that the clearance flow issues from an axial location just after the pressure side leg of the passage normal shock. This was because an abrupt pressure difference between the suction side and pressure side across the tip was caused by the passage normal shock. This indicates that the passage shock controls the spot where the tip clearance flow begins to issue on the blade tip. Note also that there is a low Mach number region indicated by concentric closed contours just behind the intersection of the passage normal shock and the tip clearance flow. The center of the region gives very distorted flow area with low Mach number values, and has only one-third momentum of those of the blade inlet main flow. This is the core of high blockage and was also pointed out by Adamczyk et al. (1993) as a "low pressure core." Figure 3(b) depicts the particle traces released in the tip gap region to show the behavior of the tip clearance flow. This figure shows evidently that the tip clearance flow which issues just after the pressure side leg of the passage normal shock rolls up into a conical vortex, that is, a tip leakage vortex. Comparison of Fig. 3(a) with Fig. 3(b) shows the shock-like line of the tip clearance flow in Fig. 3(a) is not a vortex itself, but is found to be a thin shear layer between the main flow and the tip leakage vortex. Thus we can regard this line as the border separating the tip leakage vortex region from the main flow region. This shock-like line (or the line of thin shear layer) appears as an enveloping surface of the tip leakage vortex toward the hub as far as the 96% span (not shown). Figure 3(b) also shows that the tip leakage vortex increases its diameter when it passes the passage normal shock. These features are summarized in a schematic for clarification in Fig. 3(c). The convergence history for this choke condition is given in Fig. 3(d), which indicates that the flow at this condition is steady.

The Flowfield at the Medium Condition. We term the operating point whose mass flow rate is 2.74kg/s as "medium condition" temporarily. Figure 4(a) gives the flow pattern of the medium condition (relative Mach number contours). Since the back pressure is raised from the choke condition, the passage normal shock moves upstream. As the shock moves, the spot where the tip leakage vortex begins abruptly on the blade tip and the core of high blockage which shows up as concentric closed contours also moves upstream. The passage normal shock is seen to be separated by the shear layer in the middle and movement of the upper and lower passage normal shock differ across the shear layer, which suggests strong shock-tip leakage vortex interaction. The leading edge shock and the upper and lower passage normal shock form a lambda-shock structure. This picture shows very good qualitative agreement with the Schlieren photograph by Freeman (1985). Figure 4(b) depicts the behavior of the tip clearance flow by particle traces. It shows clearly that the tip clearance flow takes a form of the tip leakage vortex again and the spot where it begins moves further upstream compared to the choke point (Fig. 3(b)). The

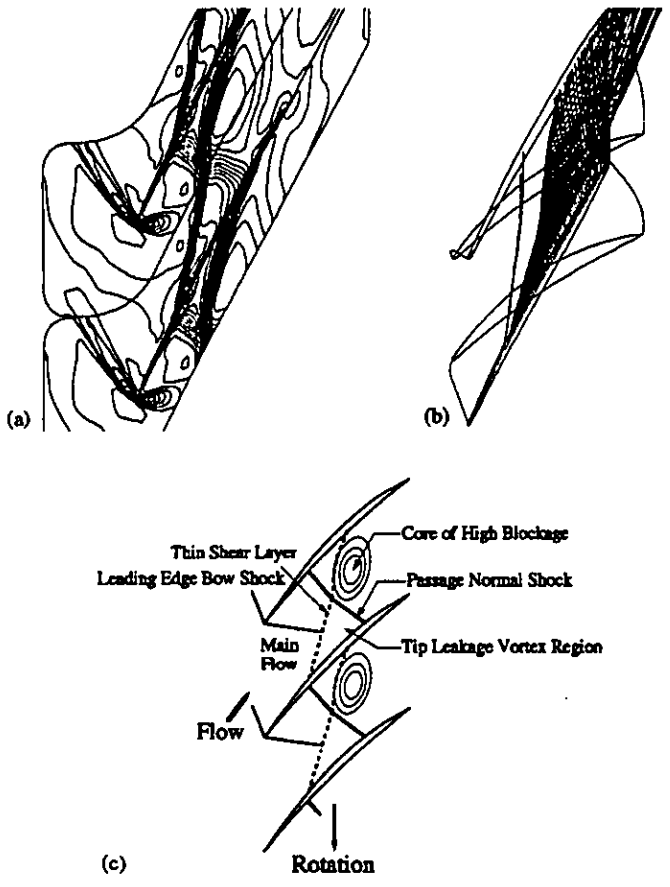

Fig. 3 Computed Flowfield of the Choke Point with 0.5% Clearance; (a)Relative Mach Number Contours in the Clearance Region (contour increment is 0.05), (b)Particle Traces Released from the Blade Tip, (c)Schematic for Clarification, (d)The Convergence History for the Choke Point

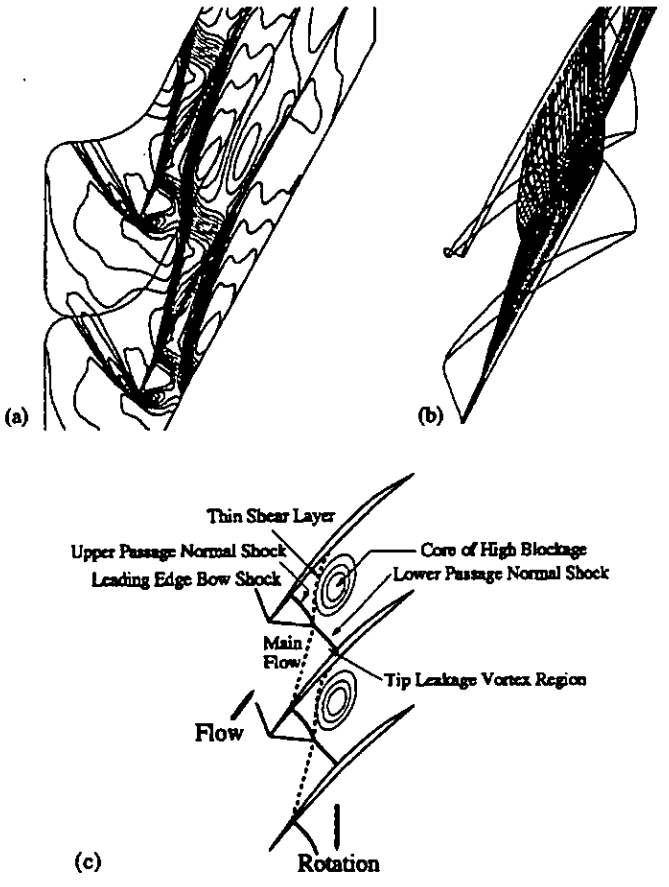

Fig. 4 Computed Flowfield of the Medium Condition with 0.5% Clearance; (a)Relative Mach Number Contours in the Clearance Region (contour increment is 0.05), (b)Particle Traces Released from the Blade Tip, (c)Schematic for Clarification, (d)The Convergence History for the Medium Condition

diameter of the tip leakage vortex grows more abruptly when it passes the passage normal shock. The distorted flow at the intersection of shock and tip leakage vortex is easily be seen from this figure, too. The large negative axial velocity components arise at the intersection. The schematic view of the medium condition is summarized in Fig. 4(c). Figure 4(d) confirms that the flow at this medium condition reaches a steady state.

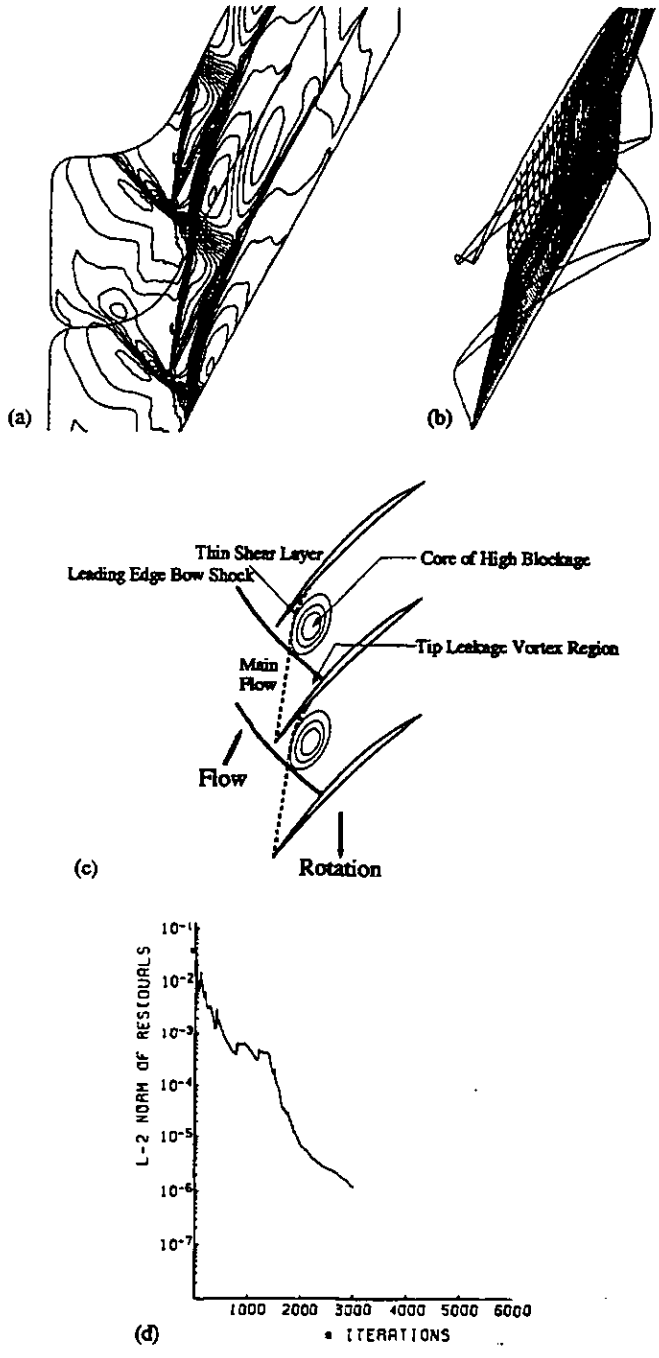

Fig. 5 Computed Flowfield of the Near-Stall Point with 0.5% Clearance; (a)Relative Mach Number Contours in the Clearance Region (contour increment is 0.05), (b)Particle Traces Released from the Blade Tip, (c)Schematic for Clarification, (d)The Convergence History for the Near-Stall Point

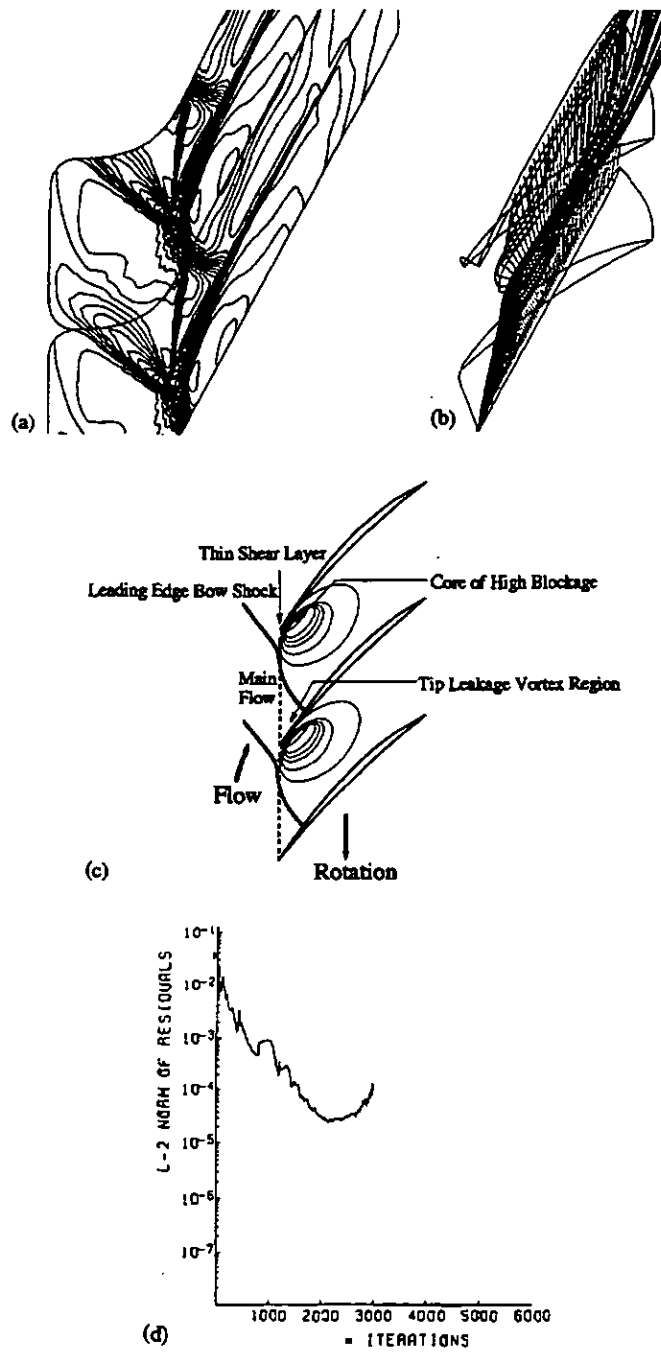

Fig. 6 Computed Flowfield of the Surge Point with 0.5% Clearance; (a)Relative Mach Number Contours in the Clearance Region (contour increment is 0.05), (b)Particle Traces Released from the Blade Tip, (c)Schematic for Clarification, (d)The Convergence History for the Surge Point

The Flowfield at the Near-Stall Point. The back pressure was raised so that the mass flow rate reduced to 2.62kg/s. With this high back pressure, as illustrated in the relative Mach number contours of Fig. 5(a), the passage normal shock could not stay within the blade passage, and was pushed ahead of the blade rows where it formed a detached leading edge bow shock. Here we call this flowfield the near-stall point. Since there is no passage shock at this condition, the tip leakage vortex does not issue

midway on the blade tip. Instead, the tip leakage vortex originates from the leading edge, as shown in Fig. 5(a), and therefore is called the leading edge vortex. Note that the concentric closed contours of the core of high blockage move further upstream following the shock motion, and are located almost at the entrance of the blade passages, also seen in Fig. 5(a). This causes the main flow to enter the blade passages at a rather high angle of attack. Figure 5(b) shows the particle traces released from the tip gap region and confirms that the leakage flow originates from the leading edge. It shows again that the particles undergo large disturbances at the core of high blockage due to the adverse pressure gradient of the detached leading edge bow shock and strengthen the negative axial velocity component at the core. The schematic of this flowfield is shown in Fig. 5(c). In spite of this considerably high back pressure, the L_2-norm residual dropped by more than four order of magnitude and the steady-state solution was obtained (Fig. 5(d)). So the flow still remained steady.

The Flowfield at the Surge Point. The back pressure was further raised from the near-stall point. The mass flow rate at this condition reduced to as much as 2.48kg/s, and we could not obtain the steady-state solution with this back pressure, as will be shown later. Figure 6(a) shows the flow pattern at the surge point expressed in relative Mach number contours. Since the back pressure was further raised from the near-stall point, the detached leading edge bow shock moved upstream a little. Note that only the suction side leg of the detached bow shock advances due to the shock-vortex interaction. The qualitative agreement on the shock shape with various measured near-stall flowfields is obtained. Since there is no issuing point for the tip leakage vortex ahead of the blade leading edge, the tip leakage vortex keeps originating from the blade leading edge as before. But the loading of the blade's forward portion increases compared to the near-stall point, the issuing angle of the leading edge vortex also increases. As a result, the line of the thin shear layer inclined further upstream, and it almost reached the tip leading edge of the adjacent blade, covering up the entire blade passage. The core of high blockage does not move upstream so much because the detached leading edge bow shock does not move upstream so much either, and the tip leakage vortex keeps originating from the leading edge as before. Or rather, it approaches the leading edge of the adjacent blade, increasing its region both pitchwise and streamwise compared to previous operating points, as can be seen from the concentric closed contours appearing in Fig. 6(a). The particle traces released from the tip gap region are depicted in Fig. 6(b). We can also see from this figure that the issuing angle of the leading edge vortex increases. Note that the vertical angle of conical vortex as well as its issuing angle increases. The disturbances the particles undergo at the core of high blockage get sn much larger that the particles are reversed as if discharged from the entrance of the blade passages. These flow features are summarized in the schematic of Fig. 6(c) . As mentioned above, the steady-state solution could not be obtained at this condition. Figure 6(d) depicts the convergence history of L_2-norm residuals, from which we can see it not only fails to converge to a steady state, but also is diverging rapidly. The process of the divergence is somewhat different from those of Adamczyk et al. (1993) and Arnone (1994). Their calculations showed the detached bow shock was driven further and further upstream and when it reached the inlet boundary of the computational domain, the calculation failed. That property may be a shortcoming since such a process of divergence makes obscure the judgement whether the calculation diverged due to tip clearance flow or due to numerical interaction between the shock driven forward and the inlet boundary. Moreover, as Adamczyk et al. (1993) reported the near-stall calculation with zero clearance where neither the tip clearance flow nor the associated forward movement of low energy fluid, (Both of them were considered to initiate stall), was seen, arguments became more confusing. Contrary to these, our calculations did not exhibit the continuous forward movement of the detached leading edge bow shock. In our calculations, the flow around the blade tip leading edge begins to oscillate and the amplitude of the oscillation keeps growing from the viewpoint of the residuals. It leads to rapid divergence of the calculation unless the time step size is changed. If the time step size is greatly reduced, it does not lead to divergence, but the flow keeps oscillating and the residuals had never dropped by as much as two orders of magnitude. In any case, these signs suggest the nonexistence of the steady flow at this condition. The cause of the discrepancy in the process of numerical divergence between the present calculation and those by Adamczyk et al. or Arnone is not known at present. This may be attributed to the difference in time step sequences.

On the Onset of the Transonic Fan/Compressor Surge. Figure 6(a) shows that the flow of this transonic compressor begins to stall when the line of the thin shear layer between the main flow and the tip leakage vortex (i.e. the edge of the tip leakage vortex) reaches the leading edge of the adjacent blade. The stall in numerical simulations cannot immediately be linked with the stall of the actual machines. But taking into account that the numerical scheme and its boundary conditions employed here were nothing special and exhibited that good numerical stability up to the surge point was reached, we consider the calculated stall as some reflection of physical phenomena not caused by numerical reasons. Comparisons of Figs. 3, 4, 5 and 6 show that the only cause which triggers the stall is obviously the impingement of the leading edge vortex on the tip leading edge of the adjacent blade. The situation looks as if the tip leading edge of the adjacent blade was captured into a fierce vortex at a considerably high angle of attack. It seems impossible for the flow through blade passages to remain steady in such situations. Also, if the edge of the leading edge vortex was pushed ahead of the leading edge of the adjacent blade, it means that the axial velocity components become

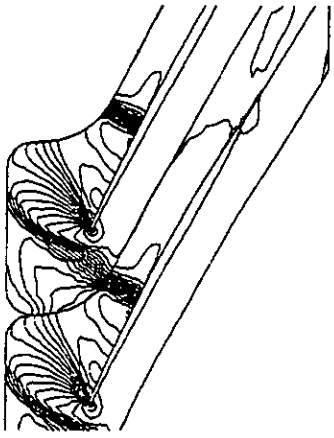

Fig. 7 Relative Mach Number Contours of a Steady Euler Solution in the Tip Region with the Mass Flow Rate of 2.22 kg/s (contour increment is 0.05)

negative in the entire front area of the blade passage around the tip region, thus the blade tip will be in complete stall. Thus, we conclude that the edge of the leading edge vortex impinging upon the adjacent blade's tip leading edge causes tip stall and its occupying that position is a geometry-independent criterion of the failure of steady flow or the onset of tip stall in typical transonic fan/compressor rotors. This is partly proved by a striking contrast of a steady Euler solution obtained with higher pressure ratio (1.84) and lower mass flow rate (2.22kg/s) than those of the surge point in Fig. 6. Figure 7 shows possible existence of steady flow with a much larger detached distance of leading edge bow shock when there is no tip leakage vortex and its associated impingement on the adjacent blade's tip leading edge.

As a consequence, we can estimate the influence of tip clearance on the surge margin. Since clearance height governs the mass flow rate through tip clearance, reduction in clearance height leads to reduction in mass flow through tip clearance, then the issuing angle and the vertical angle of the conical leading edge vortex will also be reduced, consequently the edge of the leading edge vortex will not impinge upon the adjacent blade's tip leading edge until higher pressure ratio and lower mass flow rate is reached, which will lead to the enhancement of stable operating range, and vice versa. This model can relate the measured fact that slight increase in tip clearance height leads to great reduction in stable operating range, and vice versa, to a definite flow phenomenon.

Moreover, Figure. 5(a) or 6(a) has an important significance. First of all, They show that near stall, the leading edge vortex does produce high blockage at the rotor inlet plane around the tip region, which blockage is necessary for inception and propagation of rotating stall. These figures also imply that the guiding blade in the direction of rotation is little influenced by the following blade, while the following blade is much influenced by the guiding blade through its leading edge vortex constantly. This is suggestive of propagation mechanism of rotating stall. These signs strongly suggest that tip leakage vortex (leading edge vortex) has the strong possibility of playing a direct part of triggering rotating stall of the very inception stage. If the edge of the leading edge vortex in one blade passage is pushed ahead of rotor inlet plane near stall by some non-periodic, unsteady fluid motion, that will cause the main flow angle to turn to the axially negative direction, which will lead to issuing of the leading edge vortex emitted from the following blade in the axially negative side. Then stall in tip region will propagate one after another in the circumferential direction. Note that disruption of steady flowfield on the surge line was found to be initiated by an outbreak of rotating stall at rotor tips (Day, 1991), even in high speed compressors (Day and Freeman, 1993). These results mean that onset of rotating stall is closely linked with tip clearance, because the limit of steady flow has been shown to be directly affected by tip clearance. The proposed model is consistent with these arguments, and can explain why rotating stall usually breaks out only at rotor tips, not on arbitrary radial locations.

Validation of the Proposed Model through the Numerical Experiments with Different Tip clearance Height

Numerical experiments have been performed to examine the model obtained above. Calculations have been carried out with 0.25% and 1.0% clearance while keeping the design operating speed as before. In case of 0.25% clearance, two cells were filled in the tip gap region, while four cells were filled in the clearance gap in case of 1.0% clearance. Total number of grid points are the same as those with 0.5% clearance. 9 cases were calculated and only the representative results of them are shown below.

The Transition of the Flowfield with 0.25% Clearance. The first calculation shows the flowfield with the same back pressure with 0.5% tip clearance choke point. The mass flow rate was 2.77kg/s. Comparing Mach number contours of Fig. 8(a) with Fig. 3(a), it can be readily seen that the issuing angle and the vertical angle of the conical tip leakage vortex is greatly reduced, as anticipated previously. This is because the tip leakage vortex with reduced mass flow caused by reduction in tip clearance height is pushed aside toward the blade suction surface by the main flow. Note that the passage normal shock is located slightly downstream compared to the 0.5% clearance case. This is attributed to reduced displacement thickness of tip clearance flow. So reduced tip clearance height also contributes to enhancing stability in this aspect. The particle traces of Fig. 8(b) also support these trend. Figure 8(c) depicts the convergence history of this case.

The second calculation shows the flowfield with the same back pressure with that of the 0.5% clearance surge point. The mass flow rate of this condition was 2.54kg/s. As mentioned above, with this back pressure, the simulation with 0.5% clearance underwent a divergence, and the steady-state solution could never be obtained.

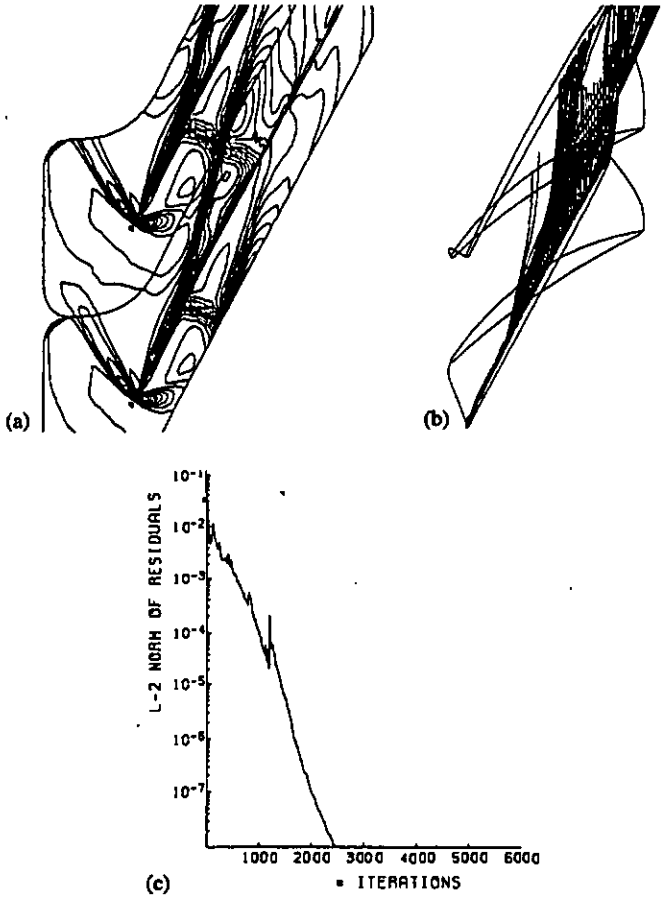

Fig. 8 Computed Flowfield of the Choke Point with 0.25% Clearance; (a)Relative Mach Number Contours in the Clearance Region (contour increment is 0.05), (b)Particle Traces Released from the Blade Tip, (c)The Convergence History for the Choke Point

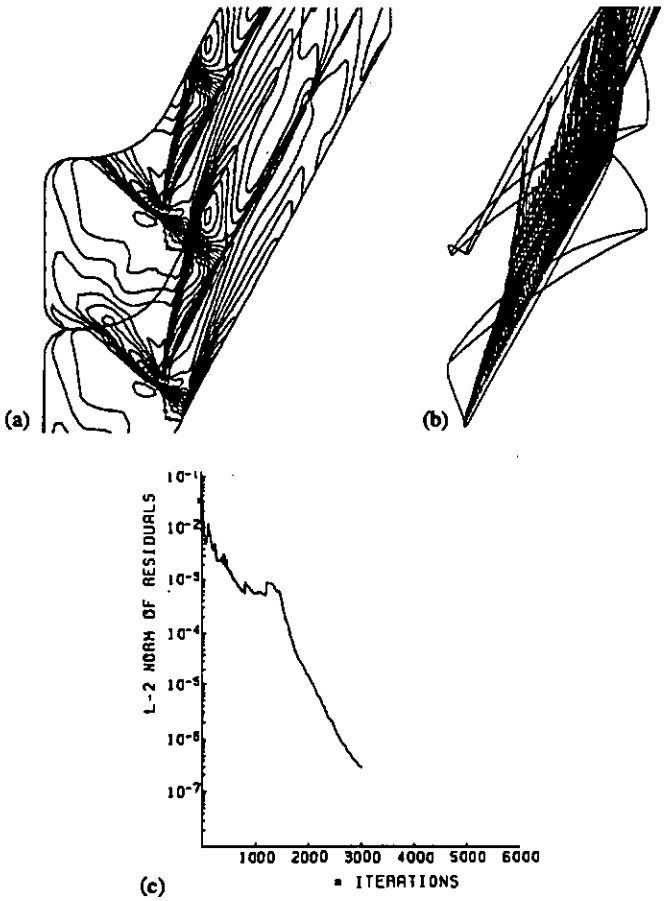

Fig. 9 Computed Flowfield with 0.25% Clearance, with the Same Back Pressure with the 0.5% Surge Point; (a)Relative Mach Number Contours in the Clearance Region (contour increment is 0.05), (b)Particle Traces Released from the Blade Tip, (c)The Convergence History for this case

The relative Mach number contours in this case are given in Fig. 9(a). The passage normal shock is pushed ahead of the blade leading edge, and the tip leakage vortex originates from the blade tip leading edge (leading edge vortex), as with the 0.5% clearance case. But the substantial difference is seen in the issuing angle of the leading edge vortex. As the issuing angle is much lower than that of the 0.5% clearance case, the edge of the leading edge vortex is far from the adjacent blade's tip leading edge and there is no covering up the entire blade passage. The core of high blockage expressed in concentric closed contours still stays around the mid passage of the blade inlet. The particle traces are shown in Fig. 9(b). All the flow features look very similar to those at near-stall point with the 0.5% clearance, i.e. Fig. 5(c), except that the issuing angle of the leading edge vortex is somewhat lower. The convergence history of this case is given in Fig. 9(c), which shows the existence of the steady-state solution and remarkable contrast with Fig. 6(d). These results support the model proposed at the last section.

The last calculation shows the surge point with 0.25% clearance. The mass flow rate at this point was 2.31kg/s, which means that the stable operating range based upon the choked mass flow rate was improved by more than 6%, compared to that of the 0.5% clearance. The relative Mach number contours in Fig. 10(a) show qualitatively similar flowfield to that in Fig. 6(a). The steady flow broke down again when the edge of the leading edge vortex impinged on the adjacent blade's tip leading edge. The particle traces of Fig. 10(b) show much more irregular motion of released particles in the core of high blockage. The convergence history exhibited very unstable behavior and the calculation stopped suddenly after fierce oscillations of residuals around the tip leading edge, as seen in Fig. 10(c). These results and those presented in Fig. 9 are considered to support strongly the model on the onset of tip stall proposed above.

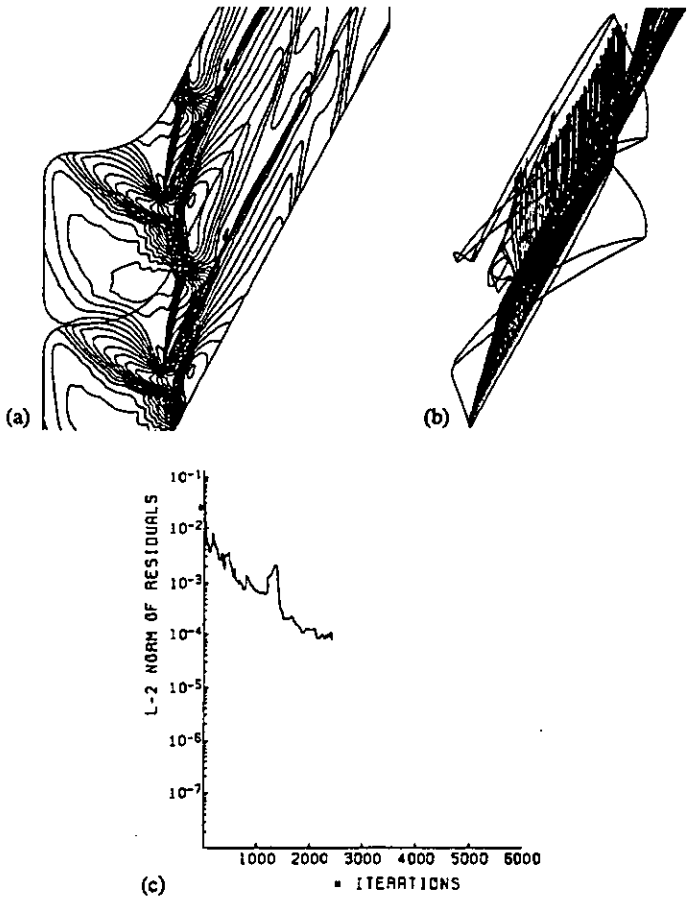

Fig. 10 Computed Flowfield of the Surge Point with 0.25% Clearance; (a)Relative Mach Number Contours in the Clearance Region (contour increment is 0.05), (b)Particle Traces Released from the Blade Tip, (c)The Convergence History for the Surge Point

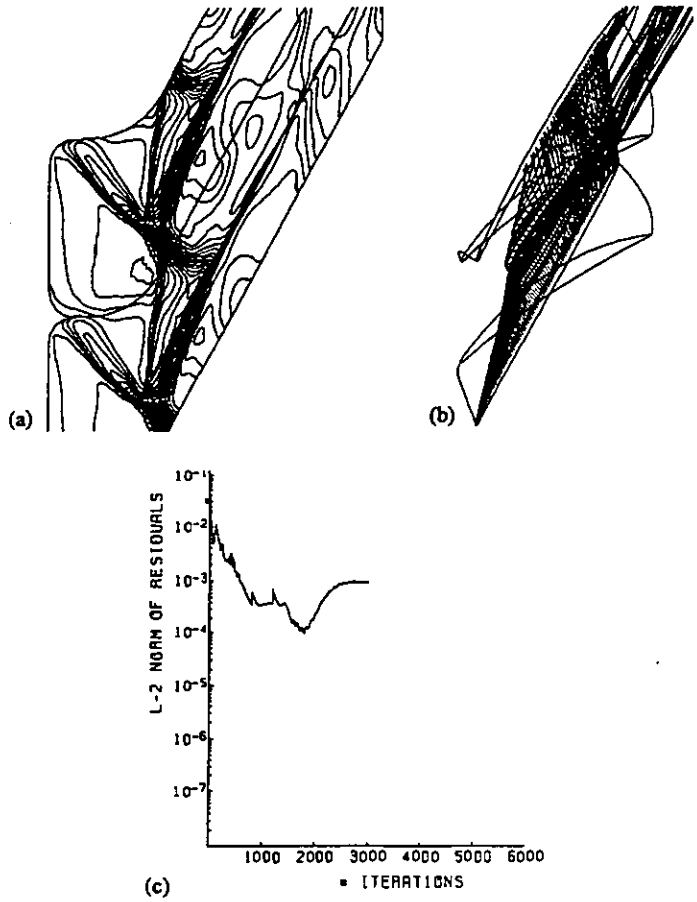

Fig. 11 Computed Flowfield of the Surge Point with 1.0% Clearance; (a)Relative Mach Number Contours in the Clearance Region (contour increment is 0.05), (b)Particle Traces Released from the Blade Tip, (c)The Convergence History for the Surge Point

The Transition of the Flowfield with 1.0% Clearance. The overall process of the transition of the flowfield with 1.0% clearance is qualitatively almost similar to those with 0.25% and 0.5% clearance, except that the passage shock and the detached leading edge bow shock diffuse more because the mass flow rate of tip clearance flow grows much higher. Also the effect of its displacement thickness becomes much larger, the shocks are likely to stand significantly more upstream, which also narrows stable operating range. At last the steady flow fails at the situation shown in Fig. 11(a), which has a qualitative resemblance with Figs 6(a) and 10(a). The particle traces of Fig. 11(b) show a locally reversed flow area in the core of high blockage, which is similar to Fig. 6(b). The convergence history shows the oscillation of large amplitude and keeps oscillating without convergence or divergence in Fig. 11(c). The model proposed in the last section is also applicable to this 1.0% clearance case.

The Influence of Tip Clearance Height on the Performance of the Transonic Compressor Rotor. All the results obtained in this research are summarized in Fig. 12 in terms of rotor total pressure ratio and rotor adiabatic efficiency. Four symbols on the 0.5% clearance characteristic indicate the choke point, the medium condition, the near-stall point, and the surge point reported in the last section, respectively. The measured and computed results are in fairly good agreement, although the objective of this research is not to demonstrate the quantitative accuracy of the code. The symbol on 0.25% clearance characteristic with almost the same pressure ratio with the 0.5% surge point correspond to the case of Fig. 9. The surge points in each case are marked with solid symbols. It can easily be seen from this figure that higher pressure rise and better peak adiabatic efficiency with greatly enhanced flow range is obtained as tip clearance height is reduced. This figure shows qualitative agreement with the measured fact that slight increase in tip clearance height reduces efficiency and stall margin greatly. The efficiency map also indicates that the

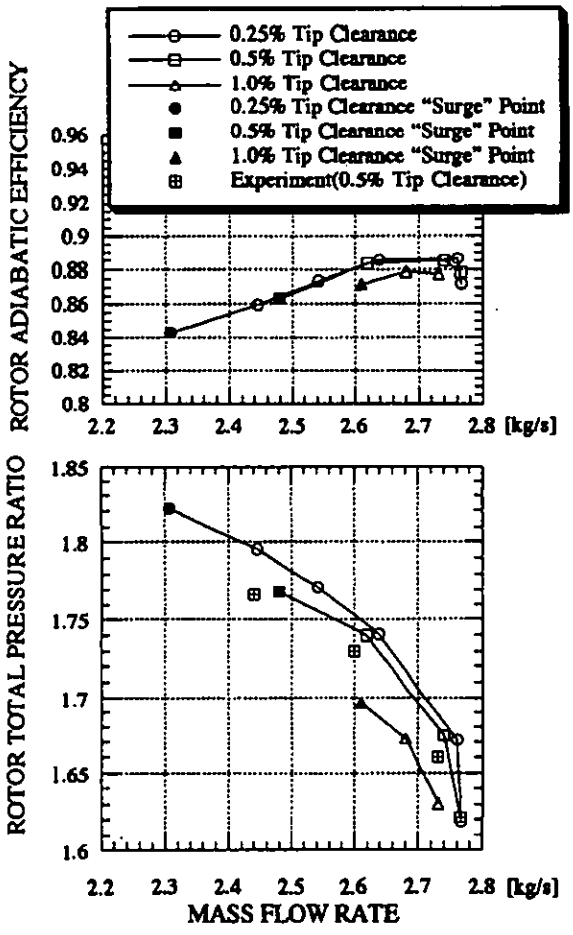

Fig. 12 A Summary of the Computed Characteristics of the Transonic Compressor Rotor at Design Operating Speed

reduction of tip clearance by less than 0.5% span does not improve efficiency substantially (improvement in stall margin is indeed gained). This may be a clue to the existence of optimum clearance with respect to efficiency and from practical point of view, the best compromise on efficiency can be obtained at 0.5% tip clearance.

SUMMARY AND CONCLUSIONS

The three-dimensional Navier-Stokes computations have been performed to reveal the flow features around the tip gap region of a transonic compressor rotor and the model on the onset of tip stall is proposed based upon these calculations. The numerical experiments were also carried out to validate this model. The conclusions drawn from these calculated results are as follows.

1. Clearance flow pattern is governed by shock pattern in transonic fan/compressor rotors. In the case of in-passage shock, tip leakage vortex issues as a jet from the suction side at an axial location just after the pressure side leg of the passage shock due to the abrupt pressure difference across the tip caused by the shock. In the case of detached leading edge bow shock, tip leakage vortex issues from the tip leading edge and further increase in the back pressure leads to increase in blade loading of the forward portion hence increase in the issuing angle of leading edge vortex.

2. There is strong interactions between tip leakage vortex and passage/leading edge shocks. Just after their intersection the core of high blockage is formed, where the flow is highly distorted.

3. The steady flow fails when the edge of leading edge vortex emitted from one blade impinges on the adjacent blade's tip leading edge. This onset of tip stall is attributed to the factor that the adjacent blade's tip leading edge is caught up in the leading edge vortex at a high angle of attack. Under such circumstances, it seems impossible for the flow through the blade passage to remain steady.

4. Near stall, the leading edge vortex does produce high blockage at the rotor inlet plane around the tip region, which blockage is necessary for inception and propagation of rotating stall. Furthermore, the guiding blade in the direction of rotation is little influenced by the following blade, while the following blade is much influenced by the guiding blade through its leading edge vortex constantly. This is suggestive of propagation mechanism of rotating stall. These signs strongly suggest that tip leakage vortex has the strong possibility of directly triggering rotating stall of the very inception stage.

5. Reduction in clearance gap results in reduction in the issuing angle and vertical angle of conical leading edge vortex. This is because tip clearance height governs the mass flow rate through it, and the tip leakage vortex with reduced mass flow caused by reduction in tip clearance height is pushed aside toward the blade suction surface by the main flow. As a consequence, the edge of the leading edge vortex does not impinge on the adjacent blade's tip leading edge until higher pressure ratio and lower mass flow rate is reached. Therefore the enhancement of flow range is obtained. On the contrary, increase in tip clearance acts adversely in all the process mentioned above, results in great reduction in flow range. This model can explain the measured fact that slight increase in tip clearance height leads to great reduction in stable operating range, and vice versa.

6. Numerical results show that tip clearance flow has a dominant influence on transonic fan/compressor rotor's stability and efficiency.

7. Reduction in tip clearance by less than 0.5% span did not exhibit substantial improvement in efficiency. This may be a clue to optimum clearance and one of criteria aimed at in the design work.

ACKNOWLEDGEMENTS

The authors would like to express their gratitude to NAL for providing computer time during the course of this work. They are also indebted to KHI for offering the blade data used herein. The first author wishes to appreciate splendid insights provided by the authors cited in this paper.

REFERENCES

Adamczyk, J. J., Celestina, M. L. and Greitzer, E. M., 1993, "The Role of Tip Clearance in High-Speed Fan Stall," ASME Journal of Turbomachinery, Vol. 115, pp. 28-39.

Arnone, A., 1994, "Viscous Analysis of Three-Dimensional Rotor Flow Using a Multigrid Method," ASME Journal of Turbomachinery, Vol. 116, pp. 435-445.

Baldwin, B. and Lomax, H., 1978, "Thin Layer Approximation and Algebraic Model for Separated Turbulent Flow," AIAA Paper 78-257.

Chima, R. V. and Yokota, J. W., 1990, "Numerical Analysis of Three-Dimensional Viscous Internal Flows," AIAA Journal, Vol. 28, pp. 798-806.

Chima, R. V., Giel, P. W. and Boyle, R. J., 1993, "An Algebraic Turbulence Model for Three-Dimensional Viscous Flows," AIAA Paper 93-0093.

Chima, R. V., 1996, "Calculation of Tip Clearance Effects in a transonic Compressor Rotor," ASME Paper 96-GT-114.

Dawes, W. N., 1988, "Development of a 3D Navier-stokes Solver for Application to All types of Turbomachinery," ASME Paper 88-GT-70.

Day, I. J., 1991, "Stall Inception in Axial Flow Compressors," ASME Paper 91-GT-86.

Day, I. J. and Freeman, C., 1993, "The Unstable Behavior of Low and High Speed Compressors," ASME Paper 93-GT-26.

Freeman, C., 1985, "Effect of Tip Clearance Flow on Compressor Stability and Engine Performance," VKI Lecture Series 1985-05.

Hah, C. and Wennerstrom, A. J., 1991, "Three-Dimensional Flowfields inside a Transonic Compressor with Swept Blades," ASME Journal of Turbomachinery, Vol. 113, pp. 241-251.

Hah, C. and Reid, L., 1992, "A Viscous Flow Study of Shock-Boundary Layer Interaction, Radial Transport, and wake Development in a Transonic compressor," ASME Journal of Turbomachinery, Vol. 114, pp. 538-547.

Jennions, I. K. and Turner, M. G., 1993, "Three-Dimensional Navier-Stokes Computations of Transonic Fan Flow Using an Explicit Flow Solver and an Implicit k-ε solver," ASME Journal of Turbomachinery, Vol. 115, pp. 261-272.

Martinelli, L. and Jameson, A., 1988, "Validation of a Multigrid Method for the Reynolds Averaged Equations," AIAA Paper 88-0414.

Masaki, D. and Kaji, S., 1994, "A Study on the Convergence of a 3-D Euler Code for Cascade Flow Calculation," NALSP-27, pp. 57-62, in Japanese.

Masaki, D., 1995, "Investigation of Flowfields in a Transonic Compressor Rotor near Stall," Ph.D. Thesis, University of Tokyo, in Japanese.

Müller, B., 1989, "Simple Improvements of an Upwind TVD Schemes for Hypersonic Flow," AIAA Paper 89-1977CP.

Roe, P. L., 1981, "Approximate Riemann Solvers, Parameter Vectors, and Difference Schemes," Journal of Computational Physics, Vol. 43, pp. 357-372.

Sorenson, R. L., 1981, "A Computer Program to Generate Two-Dimensional Grids about Airfoils and Other Shapes by the Use of Poisson's Equation," NASA TM-81198.

Strazisar, A. J., Wood, J. R., Hathaway, M. D. and Suder, K. L., 1989, "Laser Anemometer Measurements in a Transonic Axial Flow Fan Rotor," NASA TP-2897.

Yee, H. C. and Harten, A., 1987, "Implicit TVD Schemes for Hyperbolic Conservation Laws in Curvilinear Coordinates," AIAA Journal, Vol. 25, pp. 266-274.

Yee, H. C., Klopfer, G. H. and Montagne, J. -L., 1990, "High Resolution Shock-capturing Scheme for Inviscid and Viscous Hypersonic Flows," Journal of Computational Physics, Vol. 88, pp. 31-61.

Weber, K. F. and Delaney, R. A., 1991, "Viscous Analysis of Three-Dimensional Turbomachinery Flows on Body Conforming Grids Using an Implicit Solver," ASME Paper 91-GT-205.

Wisler, D. C., 1985, "Loss Reduction in Axial Flow Compressors through Low-Speed Model Testing," ASME Journal of Engineering for Gas Turbine and Power, Vol. 107, pp. 354-363.